Article

Response Evolution of a Tetrachiral Metamaterial Unit Cell under Architectural Transformations

Linar Akhmetshin *, Kristina Iokhim, Ekaterina Kazantseva and Igor Smolin

Faculty of Physics and Engineering, National Research Tomsk State University, 634050 Tomsk, Russia
* Correspondence: akhmetshin.lr@gmail.com

Abstract: This paper studies a mechanical metamaterial with tetrachiral topology by mathematical modeling. Chirality is the property of an object that makes the object distinguishable from its mirror image; chirality can be left- or right-handed. The mechanical response of two metamaterial unit cells with different configurations (patterns A and B) is investigated. It is found that the cubic cell with a regular pattern A exhibits orthotropic mechanical behavior under loading along three coordinate axes. An irregular pattern B differs from pattern A in that the upper face of the unit cell has an opposite chirality. This architectural transformation is considered as a topological defect, which enhances the twisting effect in the loaded metamaterial. Analysis of displacements and stresses shows that the mechanical behavior of the pattern B cell is described by the model of a transversely isotropic material. The orthotropic and transversely isotropic behavior of the cells of given configurations is also confirmed by the values of the effective elastic constants. Microstructural geometry and mechanical deformation of metamaterials are shown to be closely related. It is shown that a topological defect in a unit cell of a tetrachiral metamaterial strongly determines its twisting behavior.

Keywords: mechanical metamaterial; chiral structure; numerical modeling; cell connection; effective properties

1. Introduction

Three-dimensional printing technology has provided a unique opportunity to produce complex structures directly from their digital models [1,2]. The design of modern structures is often associated with metamaterials whose physical and mechanical properties depend not on the chemical composition of the base material, but on an artificially designed architecture. Metamaterials have found wide applications in engineering design of composites, porous materials, and lattice structures, which are considered as two-phase materials made up of a solid matrix and voids [3,4], as well as in biomedical applications for the fabrication of scaffolds [5].

Scaffolds can be designed from materials composed of unit cells [6]. Each cell has a certain structure and a specific characteristic. The structural properties of cells can be programmed by changing their structural parameters [7], introducing topological defects [8,9], or by the type of cell connection in a sample [10]. The first study of cubic tetrachiral cells was performed by Frenzel et al. [11]. Tetrachirality implies the presence of a node and four ligaments. Chirality is the property of an object that makes the object distinguishable from its mirror image; chirality can be left- or right-handed. The tetrachiral topology is very interesting from a design point of view due to its auxetic property [12–15]. Compared to two-dimensional (2D) chiral metamaterials, three-dimensional (3D) chiral metamaterials have a much more complex configuration and are more difficult to fabricate, so there is little research on 3D chiral auxiliary structures. Three-dimensional cubic chiral lattices were developed and numerically analyzed by Ha et al. [16]. Based on two-dimensional tetrachiral honeycombs, Fu et al. proposed a three-dimensional orthotropic chiral

structure designed by orthogonal assembling [17]. In [18,19], three-dimensional chiral and antichiral auxetic metamaterials were developed based on a novel node design with oblique load-bearing ligaments. Other three-dimensional chiral auxetic metamaterials were also proposed, e.g., in [20].

A tetrachiral structure has a nontrivial mechanical response manifested as twisting under uniaxial loading conditions. Hence, it is often difficult or even impossible to define and understand the properties of tetrachiral metamaterials. Mathematical modeling is a good time- and cost-effective research tool that can be used before the production of full-size samples. Numerical simulations also help to determine the optimal structure. Artificial intelligence algorithms show promise in this regard [21].

At present there is a large variety of structures with the load-induced twisting behavior, and the number of works exploring new structures of this type is growing [17,19,22–35]. Recently, metamaterials with rotational or torsional resonators have been proposed and investigated as a new way of highly effective vibration energy dissipation [36]. Metamaterials can also be applied to partially solve the energy crisis problems in rapidly developing countries [21]. The advantage in this case is that the use of metamaterials provides green energy solutions, which allow them to become part of the smart city ecosystem [37,38]. The given approach requires design optimization algorithms for metamaterials, and positive findings in other application areas may be useful in this regard [39,40].

Some effects produced by topological defects can be advantageous for metamaterial design. The impact of topological defects on the mechanical response of two-dimensional structures was studied by Meeussen et al. [8,9]. To our knowledge, the literature contains no reports on the influence of topological defects on (i) three-dimensional metamaterials and (ii) tetrachiral structures. This paper is intended to fill the two research gaps. First, we investigate topological defects in a three-dimensional metamaterial sample. Second, we propose considering topological defects in the form of tetrachiral structural elements with opposite chirality. Mathematical modeling is used to provide evidence that the properties of a tetrachiral metamaterial can be controlled by a topological transformation of its unit cells with chiral structure. Of special interest is to study the enhancement of the effect of structural twisting. The difference in the responses of such structures in different directions, i.e., anisotropy of their properties because of sample twisting, is considered separately.

The purpose of this work is to study the mechanical behavior of a metamaterial with a smart tetrachiral structure. The smart structure is understood here as a structure that can be modified to achieve the required mechanical properties. In other words, mechanical characteristics can be programmed, e.g., using topological defects. The mechanical response of tetrachiral unit cells of two configurations under quasi-static uniaxial loading is numerically simulated.

The rest of the paper is organized as follows: Section 2 provides the mathematical formulation, including information about the properties of the base material from which the metamaterial is built; Section 3 details the sample topology and the proposed architectural transformation; Section 4 summarizes and discusses the results obtained in this study; and Section 5 concludes the paper.

2. Materials and Methods

The boundary value problem is considered for the system of equations of elasticity theory for the fields of displacement u_i and stress σ_{ij} in a three-dimensional formulation. The system includes equilibrium Equation (1), Cauchy relations (2) for determining strains via displacements, and constitutive relations (Hooke's law) (3):

$$\nabla_j \cdot \sigma_{ij} = 0, \tag{1}$$

$$\varepsilon_{ij} = \frac{1}{2}\left(\frac{\partial u_i}{\partial x_j} + \frac{\partial u_j}{\partial x_i}\right), \tag{2}$$

$$\sigma_{ij} = \lambda \cdot \delta_{ij}\varepsilon_{kk} + 2 \cdot \mu \cdot \varepsilon_{ij}, \tag{3}$$

where σ_{ij} is the stress tensor components, ε_{ij} is the strain tensor components, x_i is the spatial coordinates, u_i is the displacement vector components, λ and μ are the Lame constants, δ_{ij} is the Kronecker delta, and i, j = 1, 2, 3.

The base material is assumed to be isotropic and homogeneous and is therefore characterized by two material constants. The elastic constants have the following values in this study: Young's modulus E = 2.6 GPa and Poisson's ratio ν = 0.4. These values correspond to acrylonitrile butadiene styrene (ABS) plastic. The effective properties of metamaterials depend to a large extent not on the elastic modulus values of the base material, but on the macrostructural geometry of the metamaterial.

Here we consider the problem of uniaxial loading of a sample made of a mechanical metamaterial. The problem was solved numerically by the finite element method using the Ansys WB 2020R2 software package. Tetrahedral finite elements were used. The size of the elements was determined from the results of the grid convergence analysis [41]. The lower face of the metamaterial sample is rigidly fixed, and the upper face is subjected to a displacement corresponding to a 3% longitudinal compression. All other faces of the sample are under free boundary conditions, which can be written as follows:

$$u_i = 0 \ \text{ for } \ x_i \in S_1, \ u_2 = -0.03l \ \text{ for } \ x_i \in S_2, \ \sigma_{ij}n_j = 0 \ \text{ for } \ x_i \in S_3, \tag{4}$$

where S_1 is the lower face, l is the size of the sample along the loading axis, S_2 is the upper face, S_3 is the side faces of the sample, and n_j is the components of the normal vector to the surface S_3.

Numerical simulations were performed by finite element modeling. A unit cell was considered as a system of rods or beams, which was modeled as a set of three-dimensional solid elements in finite element calculations. The sample was deformed without contact interactions of its constituent elements.

3. Structure of the Studied Sample

3.1. Tetrachiral Structure

Let us consider the tetrachiral element shown in Figure 1. A simple chiral element consists of a node and tangentially attached ligaments. It can have several ligaments and is named according to their number. The tetrachiral element depicted in Figure 1 has a circular node (ring) and four ligaments.
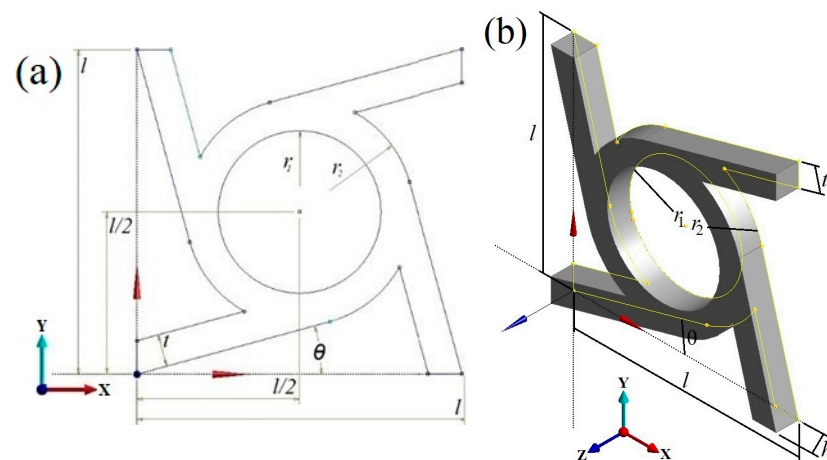

Figure 1. Tetrachiral element of the metamaterial: (**a**) two-dimensional sketch in the XY plane and (**b**) solid model.

The tetrachiral element geometry is defined by six parameters, as shown in Figure 1: l = 50 mm is the size of the square in which the element is inscribed (or the tetrachiral element size), t = 5 mm is the ligament height, h = 5 mm is the ligament thickness, r_2 = 17.5 mm is the outer ring radius, r_1 = 12.5 mm is the inner ring radius, and θ is the inclination angle of the ligament. The ligament thickness dimension in the tetrachiral element is formed when the element is extruded along the Z axis. Not all of these parameters are independent. For example, if the angle θ is measured from an imaginary line drawn tangentially from the end of the ligament to the ring, then it can be associated with the outer ring radius and the tetrachiral element size. If we assume that the ligament height coincides with the ring thickness, then the inner ring radius can be expressed in terms of the outer ring radius and the ligament height.

3.2. Topological Arrangement of Tetrachiral Elements in a Unit Cell

The tetrachiral element from Figure 1 can be considered as a wall of a three-dimensional unit cell. The porosity of the tetrachiral element is 63%. The unit cell is a cube composed of six tetrachiral elements. The porosity of the obtained unit cell is 80%. To study the possibility of modifying the mechanical properties of a metamaterial, we consider two unit cell configurations that differ only by the rotation direction of ligaments in the upper wall (Figure 2).
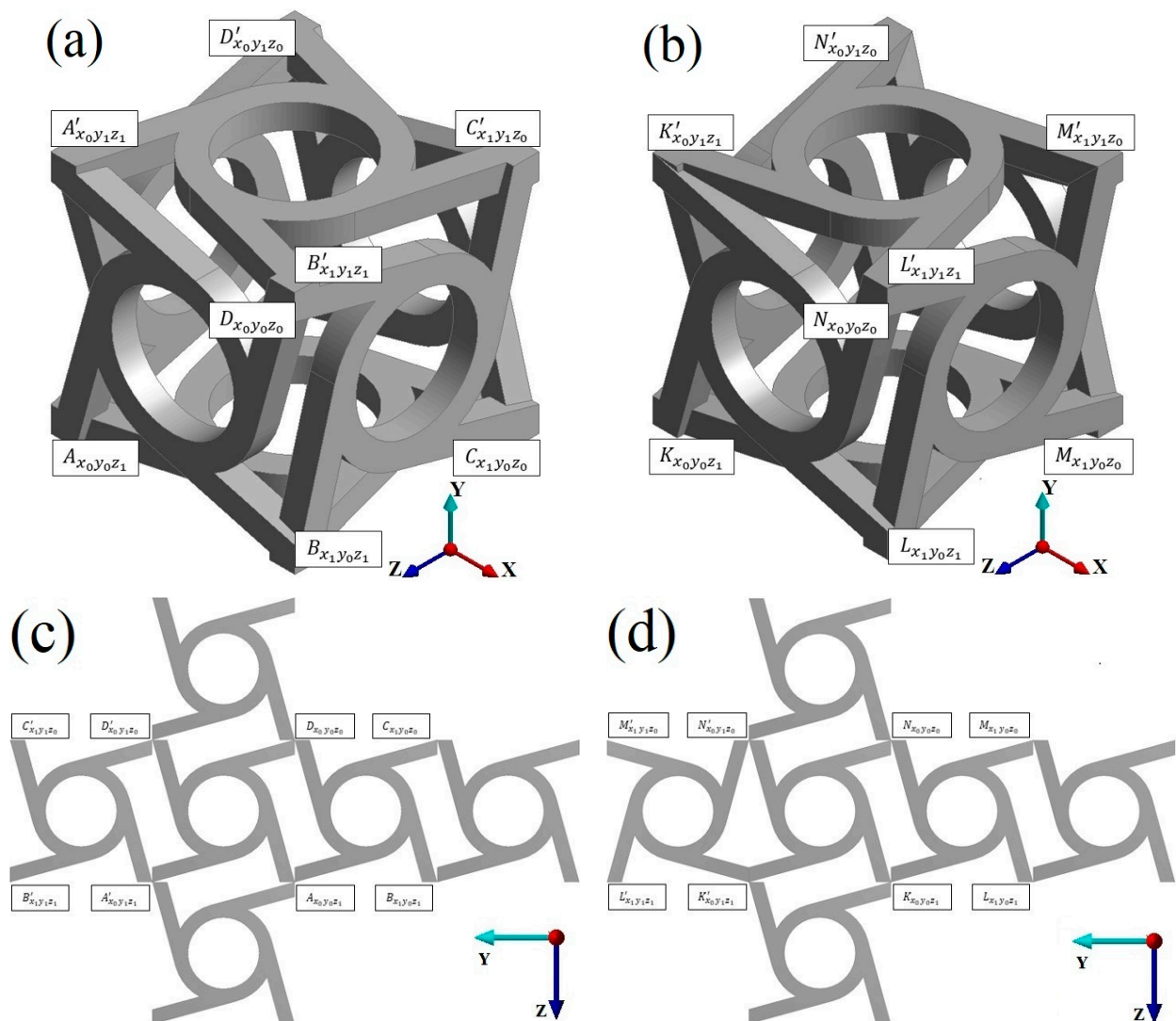

Figure 2. Two configurations of the metamaterial unit cell: (**a**,**c**) pattern A and (**b**,**d**) pattern B.

The tetrachiral elements in the unit cell of the first type (pattern A, Figure 2a) have a right-handed chirality and are arranged in such a way that the ligaments of the adjacent walls form a regular pattern. In the unit cell of the second type (pattern B, Figure 2b), the element of the upper wall has an opposite left-handed chirality and therefore breaks the pattern symmetry. These patterns can be visualized if we unfold the cubic cells onto a plane (Figure 2c,d). Since the left-handed chirality element makes the pattern irregular, it was called a topological defect.

4. Results and Discussion

4.1. Twisting

The effect of the topological defect on the mechanical behavior of the unit cell was investigated by comparing the numerical results obtained for two cell configurations. The specific feature of the tetrachiral structure design is that such a structure twists under uniaxial loading. In the three-dimensional case, the nodal points of the loaded unit cell were displaced both along the loading axis and in the plane perpendicular to this axis. In other words, the cell twisted. The cell twisting process is schematically described through point shifts (Figure 3):
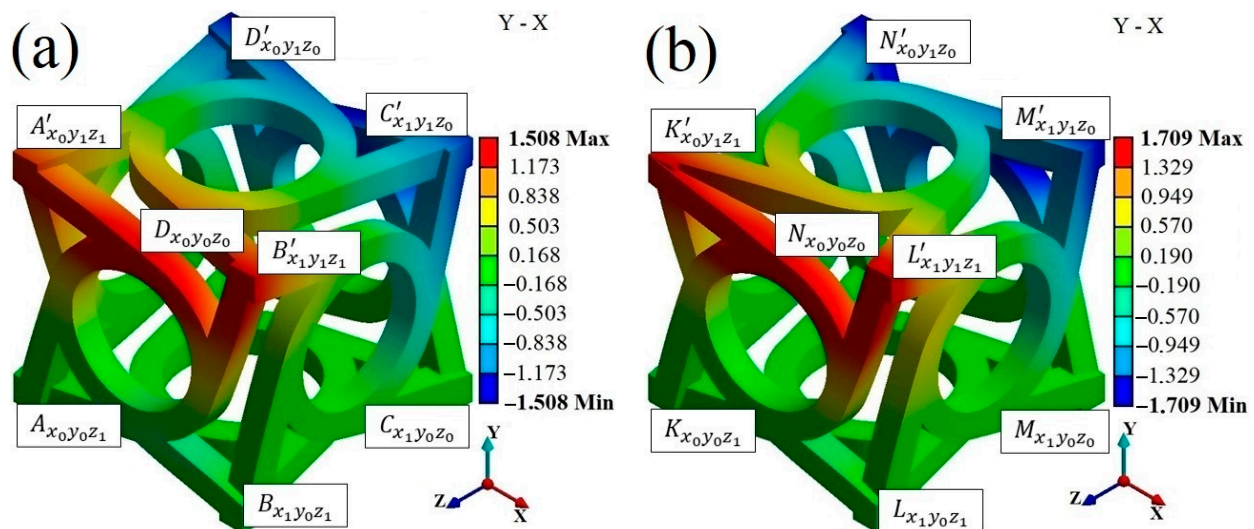

Figure 3. Vertex displacements in unit cells of two configurations: (**a**) pattern A and (**b**) pattern B.

- Nodal points A, B, C, and D (K, L, M, and N) are fixed subject to the given boundary conditions,
- Nodal points A', B', C', and D' (K', L', M', and N') move along the Y axis in accordance with the boundary conditions and are displaced in the XZ plane.

This mode of motion indicates that the 3D structure begins to twist due to the property of chirality.

Numerical calculations showed that the deviation of the considered points from the initial position in the two unit cell configurations is 13.33%. The largest displacement value can be observed in the cell with the topological defect. This result can be attributed to the rotation direction of the tetrachiral element/opposite chirality of the upper tetrachiral element. Let us consider in detail the movement of the nodal points in each of the faces, with the exception of the rigidly fixed lower face that does not participate in the movement. We can also neglect the displacement along the Y axis, as it is determined by the boundary conditions and is the same for both cells.

The direction of movement from point to point will be designated by the symbol "→".

The nodal point displacements for the regular pattern A under uniaxial compression along the *Y* axis are as follows:

Face A′B′C′D′: A′ → D′, D′ → C′, C′ → B′, B′ → A′;

Face ABB′A′: A′ → B′, B′ → B, B → A, A → A′;

Face BCC′B′: B′ → C′, C′ → C, C → B, B → B′;

Face CDD′C′: C′ → D′, D′ → D, D → C, C → C′;

Face DAA′D′: D′ → A′, A′ → A, A → D, D → D.′

The point displacements for the irregular pattern B are as follows:

Face K′L′M′N′: K′ → L′, L′ → M′, M′ → N′, N′ → K′;

Face KLL′K′: K′ → L′, L′ → L, L → K, K → K′;

Face LMM′L′: L′ → M′, M′ → M, M → L, L → L′;

Face MNN′M′: M′ → N′, N′ → N, N → M, M → M′;

Face NKK′N′: N′ → K′, K′ → K, K → N, N → N′.

Of greatest interest is the movement kinematics of the upper and adjacent side walls. One can see from the above schemes and from Figure 3 that these walls in the pattern B cell with the topological defect move in one direction. Differences in the displacement paths are underlined for clarity.

4.2. Effect of the Topological Defect on Unit Cell Behavior along Three Orthogonal Axes

The presence of the topological defect in the unit cell structure caused more pronounced twisting in the plane perpendicular to the loading axis. The mechanical behavior also changed with changing the loading axis. Figures 4 and 5 display the numerical results for loading along three orthogonal axes, showing deflections along the coordinate axes. The *X–Y* notation means that the load was applied along the *X* axis and the deviation was analyzed along the *Y* axis.
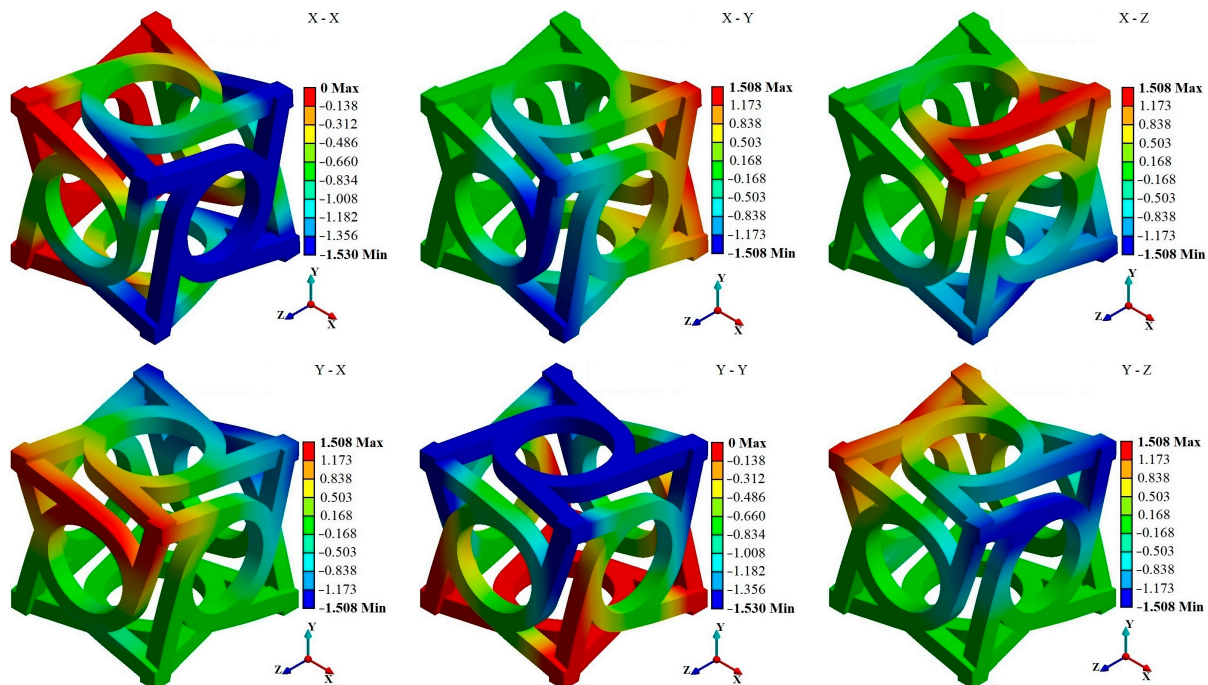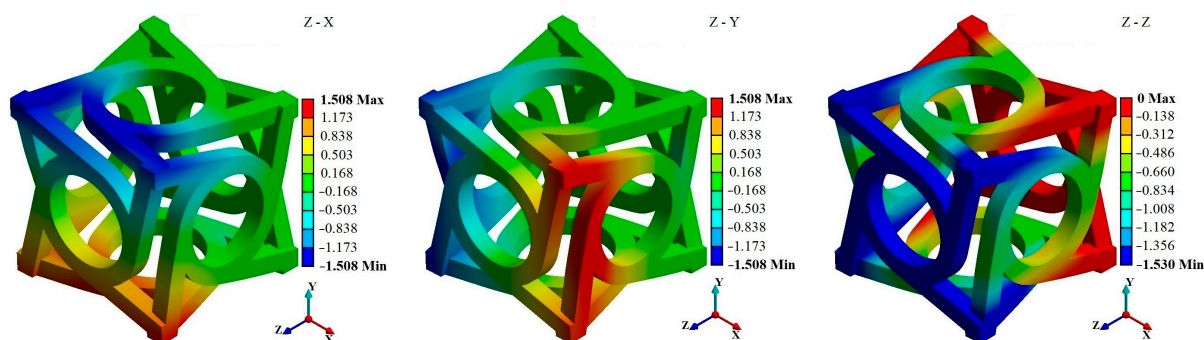
Figure 4. Mechanical behavior of the pattern A unit cell loaded along three orthogonal axes.
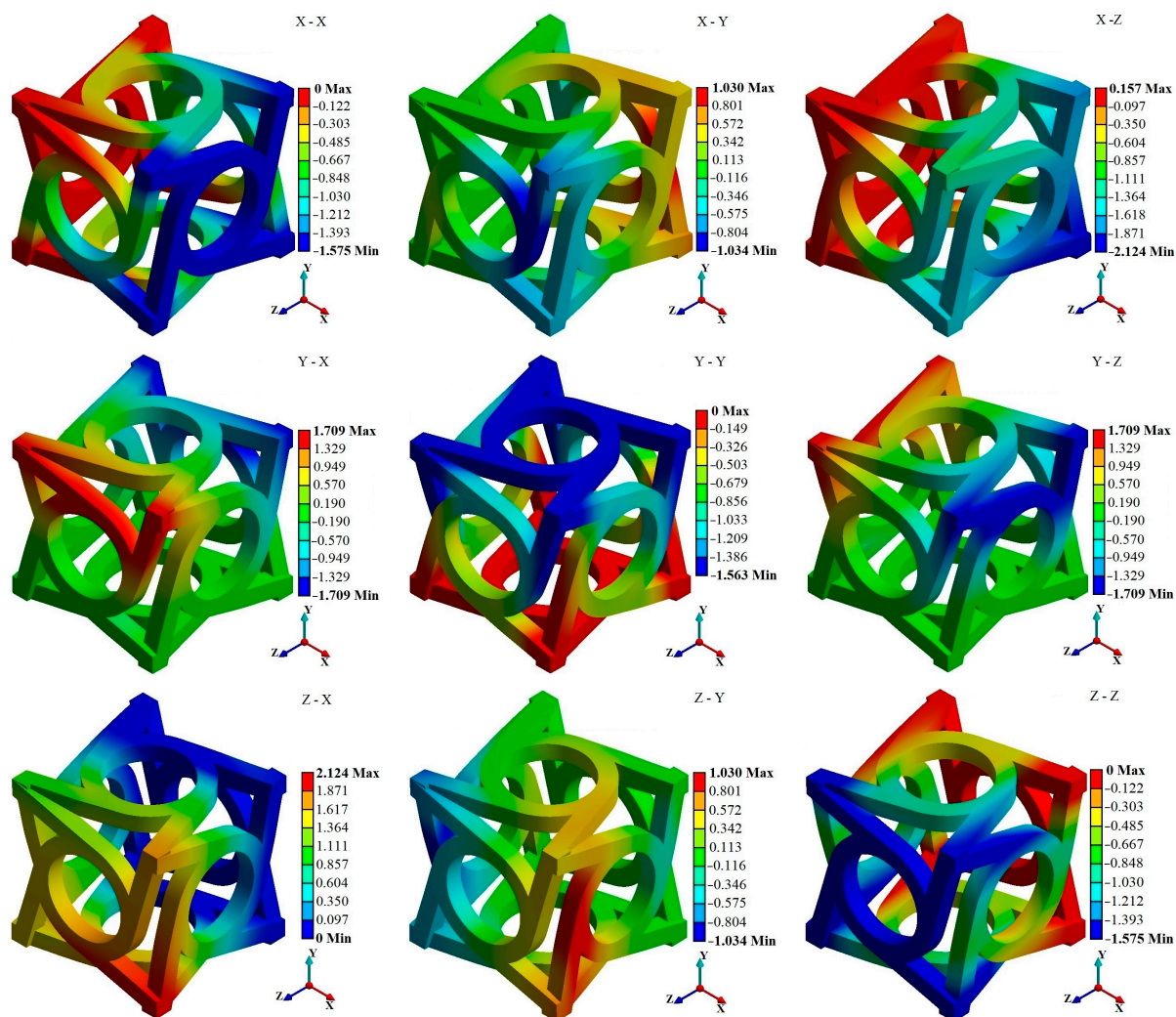

Figure 5. Mechanical behavior of the pattern B unit cell with the maximum load-induced twisting effect under loading along three orthogonal axes.

Figure 4 shows the results for the cell without a topological defect (pattern A). This configuration implies the orthotropic mechanical behavior of the unit cell. This type of behavior can be identified if we consider the deviation values, except for the cases of *X–X*, *Y–Y*, and *Z–Z*, as they correspond to the values of the boundary conditions. For all other cases, the deviation values are repeated (Figure 4). This effect is expected as a consequence of the regular tetrachiral structure pattern. The given metamaterial property can be important from the viewpoint of metamaterial-based design.

As has been shown above, the cell with a topological defect (pattern B) exhibits a more pronounced twisting effect. Numerical experiments revealed that the highest deviation value is achieved in the *X*–*Z* and *Z*–*X* cases (Figure 5), which is unexpected and not obvious. The maximum displacement in these planes is 2.124 mm, taken modulo, because one wall is shifted in the positive axis direction and the other is shifted in the negative direction during twisting. The unpredictable effect is explained by the smaller contact surface of adjacent tetrachiral elements. The least interaction between two ligaments of perpendicular walls is observed in the vertices with maximum deviation.

4.3. *Effective Poisson's Ratio*

Unit cells as a trivial case are convenient for studying the Poisson's ratio in metamaterial samples. Let us consider the effective Poisson's ratio values in a metamaterial unit cell composed of tetrachiral elements.

Regardless of the unit cell configuration (with or without a topological defect), the cell changes its shape during twisting. In this case, each cell wall is deformed in more than one plane. This is the main difficulty in determining the effective Poisson's ratio with this type of deformation. The pattern A cell exhibits comparable deviations along the *X* and *Z* axes (Figure 6). This means that there is no transverse deformation and the upper face performs a purely rotational motion. Compressional deformation along the *Y* axis is constant and nonzero in this case. Using finite difference equations [42], we can calculate strains from displacements of several points in the unit cell to determine the effective Poisson's ratios. For example, two Poisson's ratios can be determined in compression along the *Y* axis.
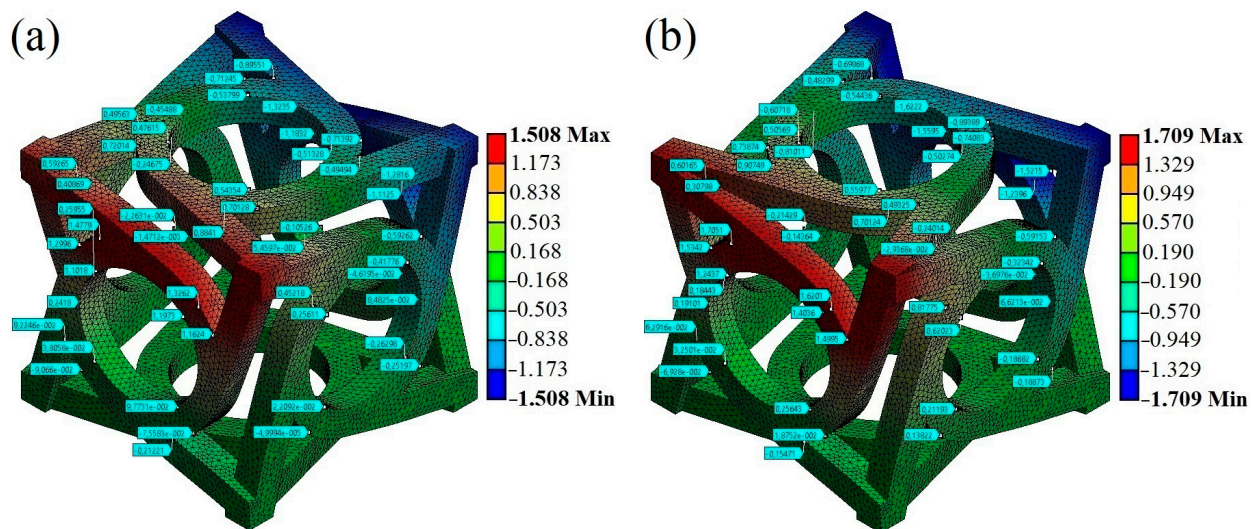

Figure 6. Selected reference points on metamaterial unit cells: pattern A (**a**) and pattern B (**b**).

$$\nu_{xy} = \frac{\varepsilon_{xx}}{\varepsilon_{yy}}, \ \nu_{zy} = \frac{\varepsilon_{zz}}{\varepsilon_{yy}}$$

The strain along the compression axis can be determined based on the given boundary conditions:

$$\varepsilon_{yy} = \frac{u_y}{l}.$$

The strains along two other orthogonal coordinate axes can be determined, e.g., from the displacements and coordinates of four points in a plane perpendicular to the loading axis using the following formulas:

$$\varepsilon_{xx} = \frac{\partial u_x}{x} = -\frac{(u_{x2} - u_{x4})(z_3 - z_1) - (u_{x3} - u_{x1})(z_2 - z_4)}{2S}$$

$$\varepsilon_{zz} = \frac{\partial u_z}{z} = \frac{(u_{z2} - u_{z4})(x_3 - x_1) - (u_{z3} - u_{z1})(x_2 - x_4)}{2S}$$

where

$$2S = (z_2 - z_4)(x_3 - x_1) - (z_3 - z_1)(x_2 - x_4).$$

Hence,

$$\nu_{xy\_A} = -\frac{(u_{x2} - u_{x4})(z_3 - z_1) - (u_{x3} - u_{x1})(z_2 - z_4)}{(z_2 - z_4)(x_3 - x_1) - (z_3 - z_1)(x_2 - x_4)} \frac{l}{u_y}$$

Calculations with this equation were carried out for groups of four selected points on different faces, as indicated in Figure 6a. The estimates of the effective Poisson's ratio on the upper face were ν_{xy} = 0.078 and ν_{zy} = 0.078.

Other Poisson's ratios were calculated similarly: ν_{yx} = 0.078, ν_{zx} = 0.078, ν_{yz} = 0.078, and ν_{xz} = 0.078. The results obtained confirm that the pattern A cells are orthotropic, and the Poisson's ratio values are close to zero.

Now let us consider the compression of the pattern B cell along the Y axis. The cell has a fourfold rotational symmetry axis, so the equality $\nu_{xy} = \nu_{zy}$ also holds for it. The effective Poisson's ratios estimated by the above equations have the following values: ν_{xy} = −0.046, ν_{zy} = −0.046, ν_{yx} = −0.141, ν_{zx} = 0.380, ν_{yz} = −0.142, and ν_{xz} = 0.380. This means that the estimates correspond to the model of a transversely isotropic body with the XZ isotropic plane.

4.4. Effective Young's Modulus

The effective Young's moduli for the two studied unit cell configurations were estimated by analyzing the support reaction force of the fixed wall under loading along three coordinate axes (Figure 6). Pattern A maintains a constant value for the three coordinate axes due to the orthotropic behavior of the cell. In the case of pattern B, the greatest reaction force is observed under loading along the Y axis. This effect is caused by the embedded topological defect that prevents adjacent tetrachiral elements from rotating. As a result, compression of the sample to the same strain requires greater force.

Knowing the support reaction, the effective Young's modulus for all loading scenarios and for both cell configurations can be determined by the following formulas:

$$E_{A_x} = E_{A_y} = E_{A_z} = \frac{\frac{F}{S}}{\frac{\Delta l}{l}} = \frac{\frac{1732.7}{25 \times 10^{-6}}}{\frac{15 \times 10^{-4}}{5 \times 10^{-3}}} = 0.231 \, \text{GPa}$$

$$E_{B_x} = \frac{\frac{F}{S}}{\frac{\Delta l}{l}} = \frac{\frac{2324.4}{25 \times 10^{-6}}}{\frac{15 \times 10^{-4}}{5 \times 10^{-3}}} = 0.310 \, \text{GPa}$$

$$E_{B_y} = \frac{\frac{F}{S}}{\frac{\Delta l}{l}} = \frac{\frac{2669.2}{25 \times 10^{-6}}}{\frac{15 \times 10^{-4}}{5 \times 10^{-3}}} = 0.356 \, \text{GPa}$$

$$E_{B_z} = \frac{\frac{F}{S}}{\frac{\Delta l}{l}} = \frac{\frac{2323.9}{25 \times 10^{-6}}}{\frac{15 \times 10^{-4}}{5 \times 10^{-3}}} = 0.310 \, \text{GPa}$$

The Young's modulus values for pattern B along the Y axis were 15% larger than those for pattern B along the X and Z axes. The Young's moduli for pattern A along all

three axes were the same and turned out to be lower by 54% compared to the Young's modulus for pattern B along the *Y* axis.

4.5. Equivalent Stress Distribution

This section analyzes the local stress values for the two studied configurations. Figure 7 shows the distributions of equivalent stresses (von Mises stresses) in the cells loaded along three orthogonal axes. The stress distributions in the pattern A cell confirm its orthotropic behavior. The maximum stresses are observed at the wall junctions and in the contact areas between ligaments and rings in the tetrachiral elements.
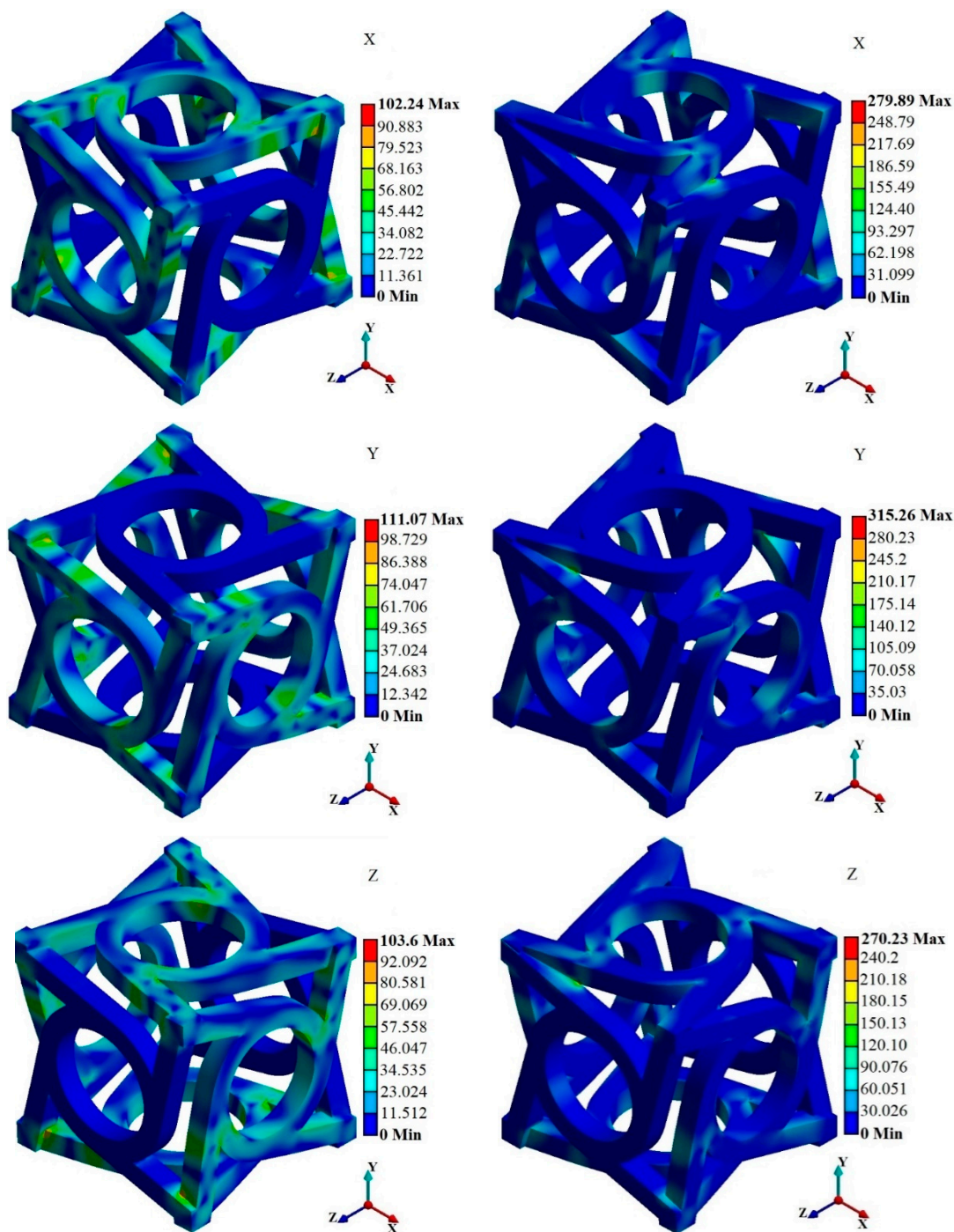
Figure 7. Equivalent stress distributions under loading along three orthogonal coordinate axes.

Pattern B is characterized by a more inhomogeneous stress distribution, with stronger stress concentrators at the junctions between the upper and adjacent walls. Attention should be paid to the contact areas not only between the upper and adjacent walls, but also between ligaments and rings. The topological defect in pattern B can be considered as a nonoptimal metamaterial design, leading to the appearance of additional strain localization regions with maximum equivalent stresses. One can see that the maximum value of equivalent stresses is higher by a factor of three compared to pattern A. The stress distributions under loading along the X and Z axes are similar, indicating the transversely isotropic behavior of the pattern B cell.

5. Conclusions

This paper studied the behavior of two cubic metamaterial unit cells of different configurations (patterns A and B) with walls formed by tetrachiral elements. The difference was that the upper wall in one of the cells had an opposite chirality. It was shown that this design feature can be interpreted as a topological defect. The twisting behavior of the unit cells was discussed for the case of uniaxial loading conditions.

Numerical experiments showed that the pattern A cell has the same physical and mechanical characteristics when loaded along three orthogonal axes. This suggests that the cell exhibits orthotropic mechanical behavior.

The pattern B cell was modified in order to increase the twisting effect. The chirality of its upper wall was reversed in such a way as to satisfy the condition of increasing the load-induced twisting effect in the XZ plane under loading along the Y axis. The opposite chirality of the upper wall was considered as a topological defect in pattern B, which was visualized by unfolding the cubic cell onto a plane. The topological defect was shown to increase the twisting degree of the cell by 13%.

The symmetry of pattern B was broken by the topological defect, and as a result the unit cell was no longer orthotropic. Further analysis of the cell showed an unexpected result: the maximum displacement values were observed along the Z axis under loading along the X axis and along the X axis under loading along the Z axis, being equal to $d_{x\text{-}z}$ = −2.124 mm and $d_{z\text{-}x}$ = 2.124 mm.

Equivalent stress distributions were also analyzed for patterns A and B. Characteristic stress distributions for each of the three loading axes confirmed the orthotropic mechanical behavior of the pattern A cell and the transversely isotropic behavior of the pattern B cell. The maximum stress values in the pattern B cell were about three times higher than for pattern A.

The obtained results confirm the close relationship between microstructural geometry and mechanical deformation. The introduction of topological defects into metamaterial structures plays a key role in the control of their behavior. It was shown that a topological defect in a unit cell of a tetrachiral metamaterial strongly determines its twisting behavior.

References

1. Ullah, A.; Kiuno, H.; Kubo, A.; D'Addona, D.M. A system for designing and 3D printing of porous structures. *CIRP Ann.* **2020**, *69*, 113–116. https://doi.org/10.1016/j.cirp.2020.04.088.

2. Hanks, B.; Berthel, J.; Frecker, M.; Simpson, T.W. Mechanical properties of additively manufactured metal lattice structures: Data review and design interface. *Addit. Manuf.* **2020**, *35*, 101301. https://doi.org/10.1016/j.addma.2020.101301.

3. Ji, S.; Gu, Q.; Xia, B. Porosity dependence of mechanical properties of solid materials. *J. Mater. Sci.* **2006**, *41*, 1757–1768. https://doi.org/10.1007/s10853-006-2871-9.

4. Pan, C.; Han, Y.; Lu, J. Design and Optimization of Lattice Structures: A Review. *Appl. Sci.* **2020**, *10*, 6374. https://doi.org/10.3390/app10186374.

5. Abbasi, N.; Hamlet, S.; Love, R.M.; Nguyen, N.-T. Porous scaffolds for bone regeneration. *J. Sci. Adv. Mater. Devices* **2020**, *5*, 1–9. https://doi.org/10.1016/j.jsamd.2020.01.007.

6. Seto, Yu.; Ullah, Sh.; Kubo, A.; D'Addona, D.M.; Teti, R. On the Porous Structuring using Unit Cells. *Procedia CIRP* **2021**, *99*, 381–386. https://doi.org/10.1016/j.procir.2021.03.054.

7. Akhmetshin, L.R.; Smolin, I.Yu. Influence of unit cell parameters of tetrachiral mechanical metamaterial on its effective properties. *Nanosci. Technol. Int. J.* **2020**, *11*, 265–273. https://doi.org/10.1615/NanoSciTechnolIntJ.2020033737.

8. Meeussen, A.S.; Oğuz, E.C.; Shokef, Y.; Hecke, M. Topological defects produce exotic mechanics in complex metamaterials. *Nat. Phys.* **2019**, *16*, 307–311. https://doi.org/10.1038/s41567-019-0763-6.

9. Meeussen, A.S.; Oğuz, E.C.; Hecke, M.; Shokef, Y. Response evolution of mechanical metamaterials under architectural transformations. *New J. Phys.* **2020**, *22*, 023030. https://doi.org/10.1088/1367-2630/ab69b5.

10. Akhmetshin, L.R.; Smolin, I.Y. Analysis of Stress and Strain in the Tetrachiral Metamaterial with Different Kinds of Unit Cell Connections. *Procedia Struct. Integr.* **2022**, *35*, 247–253. https://doi.org/10.1016/j.prostr.2021.12.071.

11. Frenzel, T.; Kadic, M.; Wegener, M. Three-dimensional mechanical metamaterials with a twist. *Science* **2017**, 358, 1072–1074. https://doi.org/10.1126/science.aao4640.

12. Bryukhanov, I.A.; Gorodtsov, V.A.; Lisovenko, D.S. Atomistic Modeling of the Mechanical Properties of Chiral Metallic Nanotubes. *Phys. Mesomech.* **2020**, *23*, 477–486. https://doi.org/10.1134/S102995992006003X.

13. Surjadi, J.U.; Gao, L.; Du, H.; Li, X.; Xiong, X.; Fang, N.X.; Lu, Y. Mechanical metamaterials and their engineering applications. *Adv. Eng. Mater.* **2019**, *21*, 1800864. https://doi.org/10.1002/adem.201800864.

14. Cho, H.; Seo, D.; Kim, D.N. Mechanics of Auxetic Materials. In *Handbook of Mechanics of Materials*; Schmauder, S., Chen, C.S., Chawla, K., Chawla, N., Chen, W., Kagawa, Y., Eds.; Springer: Singapore, 2018. https://doi.org/10.1007/978-981-10-6855-3_25-1.

15. Ren, X.; Das, R.; Tran, Ph.; Ngo, T.D.; Xie, Y.M. Auxetic metamaterials and structures: A review. *Smart Mater. Struct.* **2018**, *27*, 023001. https://doi.org/10.1088/1361-665X/aaa61c.

16. Ha, C.S.; Plesha, M.E.; Lakes, R.S. Chiral three-dimensional lattices with tunable Poisson's ratio. *Smart Mater. Struct.* **2016**, *25*, 054005. https://doi.org/10.1088/0964-1726/25/5/054005.

17. Fu, M.; Zheng, B.; Li, W. A novel chiral three-dimensional material with negative Poisson's ratio and the equivalent elastic parameters. *Compos. Struct.* **2017**, *176*, 442–448. https://doi.org/10.1016/J.COMPSTRUCT.2017.05.027.

18. Fu, M.; Liu, F.; Hu, L. A novel category of 3D chiral material with negative Poisson's ratio. *Compos. Sci. Technol.* **2018**, *160*, 111–118. https://doi.org/10.1016/J.COMPSCITECH.2018.03.017.

19. Ebrahimi, H.; Mousanezhad, D.; Nayeb-Hashemi, H.; Norato, J.; Vaziri, A. 3D cellular metamaterials with planar anti-chiral topology. *Mater. Des.* **2018**, *145*, 226–231. https://doi.org/10.1016/J.MATDES.2018.02.052.

20. Duan, S.; Xi, L.; Wen, W.; Fang, D. A novel design method for 3D positive and negative Poisson's ratio material based on tension-twist coupling effects. *Compos. Struct.* **2020**, *236*, 111899. https://doi.org/10.1016/j.compstruct.2020.111899.

21. Ghadami, N.; Gheibi, M.; Kian, Z.; Faramarz, M.G.; Naghedi, R.; Eftekhari, M.; Fathollahi-Fard, A.M.; Dulebenets, M.A.; Ти아т, G. Implementation of solar energy in smart cities using an integration of artificial neural network, photovoltaic system and classical Delphi methods. *Sustain. Cities Soc.* **2021**, *74*, 103149. https://doi.org/10.1016/j.scs.2021.103149.

22. Sabouni-Zawadzka, A.A.; Gilewski, W. Smart Metamaterial Based on the Simplex Tensegrity Pattern. *Materials* **2018**, *11*, 673. https://doi.org/10.3390/ma11050673.

23. Jiang, Y.; Li, Y. Novel 3D-Printed Hybrid Auxetic Mechanical Metamaterial with Chirality-Induced Sequential Cell Opening Mechanisms. *Adv. Eng. Mater.* **2017**, *20*, 1700744. https://doi.org/10.1002/adem.201700744.

24. Zhong, R.; Zheng, B.; Fu, M. A Novel Strategy for Constructing 3D Dislocated Chiral Metamaterial with Negative Poisson's Ratio. *Adv. Eng. Mater.* **2021**, *23*, 2000991. https://doi.org/10.1002/adem.202000991.

25. Sang, S.; Wang, Z. A design of elastic metamaterials with multi-negative pass bands. *Acta Mech.* **2018**, *229*, 2647–2655. https://doi.org/10.1007/s00707-018-2128-0.

26. Mizzi, L.; Spaggiari, A. Novel chiral honeycombs based on octahedral and dodecahedral Euclidean polygonal tessellations. *Int. J. Solids Struct.* **2022**, *238*, 111428. https://doi.org/10.1016/j.ijsolstr.2022.111428.

27. Zheng, B.-B.; Zhong, R.-Ch.; Chen, X.; Fu, M.-H.; Hu, L.-L. A novel metamaterial with tension-torsion coupling effect. *Mater. Des.* **2019**, *171*, 107700. https://doi.org/10.1016/j.matdes.2019.107700.

28. Zhong, R.; Fu, M.; Chen, X.; Zheng, B.; Hu, L. A novel three-dimensional mechanical metamaterial with compression torsion properties. *Compos. Struct.* **2019**, *226*, 111232. https://doi.org/10.1016/j.compstruct.2019.111232.

29. Ziemke, P.; Frenzel, T.; Wegener, M.; Gumbsch, P. Tailoring the characteristic length scale of 3D chiral mechanical metamaterials. *Extrem. Mech. Lett.* **2019**, *32*, 100553. https://doi.org/10.1016/j.eml.2019.100553.

30. Dong, J.; Chen, W.; Zeng, Z.; Qin, Q.-H.; Xiao, Y. Analysis of wave band gaps in mechanical metamaterial based on Nelder–Mead method. *Eng. Anal. Bound. Elem.* **2019**, *103*, 109–115. https://doi.org/10.1016/j.enganabound.2019.03.011.

31. Chen, W.; Huang, X. Topological design of 3D chiral metamaterials based on couple-stress homogenization. *J. Mech. Phys. Solids* **2019**, *131*, 372–386. https://doi.org/10.1016/j.jmps.2019.07.014.

32. Zheng, B.; Liu, Y.; Liu, J.; Yin, S.; Xu, J. Novel mechanical behaviors of DNA-inspired helical structures with chirality. *Int. J. Mech. Sci.* **2019**, *161–162*, 105025. https://doi.org/10.1016/j.ijmecsci.2019.105025.

33. Li, X.; Yang, Zh.; Lu, Z. Design 3D metamaterials with compression-induced-twisting characteristics using shear–compression coupling effects. *Extrem. Mech. Lett.* **2019**, *29*, 100471. https://doi.org/10.1016/j.eml.2019.100471.

34. Wang, L.; Liu, H.-T. 3D compression–torsion cubic mechanical metamaterial with double inclined rods. *Extrem. Mech. Lett.* **2020**, *37*, 100706. https://doi.org/10.1016/j.eml.2020.100706.

35. Wang, L.; An, M.-R.; Liu, H.-T. Compression spin bio-inspired arm: A conceptual model based on compression–torsion cubic mechanical metamaterials with variable cross-section. *Extrem. Mech. Lett.* **2020**, *41*, 101069. https://doi.org/10.1016/j.eml.2020.101069.

36. Li, Y.; Zhang, H. Band gap mechanism and vibration attenuation characteristics of the quasi-one-dimensional tetra-chiral metamaterial. *Eur. J. Mech. —A/Solids* **2022**, *92*, 104478. https://doi.org/10.1016/j.euromechsol.2021.104478.

37. Shahsavar, M.M.; Akrami, M.; Gheibi, M.; Kavianpour, B.; Fathollahi-Fard, A.M.; Behzadian, K. Constructing a smart framework for supplying the biogas energy in green buildings using an integration of response surface methodology, artificial intelligence and petri net modelling. *Energy Convers. Manag.* **2021**, *248*, 114794. https://doi.org/10.1016/j.enconman.2021.114794.

38. Ni, S.; Liu, H.; Li, Q.; Quan, H.; Gheibi, M.; Fathollahi-Fard, A.M.; Tian, G. Assessment of the engineering properties, carbon dioxide emission and economic of biomass recycled aggregate concrete: A novel approach for building green concretes. *J. Clean. Prod.* **2022**, *365*, 132780. https://doi.org/10.1016/j.jclepro.2022.132780.

39. Asghari, M.; Fathollahi-Fard, A.M.; Mirzapour Al-e-hashem, S.M.J.; Dulebenets, M.A. Transformation and Linearization Techniques in Optimization: A State-of-the-Art Survey. *Mathematics* **2022**, *10*, 283. https://doi.org/10.3390/math10020283.

40. Gheibi, M.; Eftekhari, M.; Tabrizi, M.G.; Fathollahi-Fard, A.M.; Tian, G. Mechanistic evaluation of cationic dyes adsorption onto low cost calcinated aerated autoclaved concrete wastes. *Int. J. Environ. Sci. Technol.* **2021**, *19*, 6429–6444. https://doi.org/10.1007/s13762-021-03576-9.

41. Akhmetshin, L.R.; Smolin, I.Y.Analysis of some methods of integration of cells in a mechanical metamaterial. *Tomsk. State Univ. J. Math. Mech.* **2022**, *77*, 27–37. https://doi.org/10.17223/19988621/77/3.

42. Wilkins, M.L. *Computer Simulation of Dynamic Phenomena*; Springer: Berlin, Germany, 1999.